Proton-induced reactions on molybdenum

E. Lamere,[1,2,*] M. Couder,[1,†] M. Beard,[1,‡] A. Simon,[1] A. Simonetti,[3] M. Skulski,[1] G. Seymour,[1] P. Huestis,[1] K. Manukyan,[1] Z. Meisel,[4] L. Morales,[1] M. Moran,[1] S. Moylan,[1] C. Seymour,[1] and E. Stech[1]

[1]*Department of Physics, University of Notre Dame, Notre Dame, Indiana 46556, USA*

[2]*Department of Physics and Applied Physics, University of Massachusetts Lowell, Lowell, Massachusetts 01854, USA*

[3]*Department of Civil & Environmental Engineering & Earth Sciences, University of Notre Dame, Notre Dame, Indiana 46556, USA*

[4]*Institute of Nuclear & Particle Physics, Department of Physics & Astronomy, Ohio University, Athens, Ohio 45701, USA*

(Received 17 March 2019; published 19 September 2019)

Cross sections for 34 proton-induced nuclear reactions on isotopically enriched molybdenum ($^{92,94-98,100}$Mo) leading to production of ^{92}Tc, ^{93m}Tc, ^{93g}Tc, ^{94m}Tc, ^{94g}Tc, ^{95m}Tc, ^{95g}Tc, $^{96m+g}$Tc, ^{97m}Tc, ^{99m}Tc, ^{101}Tc, $^{91(m+g)}$Mo, ^{93m}Mo, ^{99}Mo, ^{89m}Nb, ^{89g}Nb, ^{91m}Nb, ^{92m}Nb, ^{95m}Nb, ^{95g}Nb, ^{96}Nb, and $^{97m+g}$Nb were measured in the energy range 8–19 MeV with the activation method using individual irradiations. The experimental data were compared with published data from natural abundance and isotopically enriched targets as well as with the predictions of the nuclear reaction code TALYS. Special attention was given to the medically relevant ^{100}Mo$(p, 2n)^{99m}$Tc and ^{100}Mo$(p, pn)^{99}$Mo as well as nine reaction cross sections that had not previously been measured in this energy range.

DOI: 10.1103/PhysRevC.100.034614

I. INTRODUCTION

One of the most widely used radioisotopes for medical diagnostics is ^{99m}Tc [1–3]. The vast majority of ^{99m}Tc is currently obtained as a decay product of ^{99}Mo produced by fission of ^{235}U enriched targets in nuclear reactors. Various alternative methods of production of ^{99}Mo and/or ^{99m}Tc have been proposed over the past two decades [4–7] to replace aging production infrastructure and to minimize the use of highly enriched uranium. One of the proposed methods for direct ^{99m}Tc production, ^{100}Mo$(p, 2n)^{99m}$Tc, has been identified as a promising approach for supplementing local supplies [8–11]. While the cross section of this direct method of production has been measured in detail, and is summarized in Ref. [12], significant questions remain to be addressed [13]. As the process to extract ^{99m}Tc from the production target material is not isotopically selective, one of the most fundamental concerns is the characterization of the coproduction of various technetium isotopes from reactions on other stable molybdenum species inherently present in the ^{100}Mo target [14–18].

Previous studies of p + Mo reactions employing natural abundance targets have been limited by the multiple overlapping (p, xn) channels present. Without detailed experimental excitation curves for each isotope, feasibility studies have been restricted to extrapolating from theoretical tools. The study of Hou *et al.* [18] evaluates the impact of molybdenum contaminants in the target material on patient dose but relies exclusively on cross section calculations. The prevailing sentiment is that such calculations are within a factor of 3 for Maxwellian averaged (n, γ) cross sections on stable nuclei [19]. For charged particle reactions the variation between different reaction codes and the accuracy of predicted reaction rates is known to vary by even larger margins [20,21]. Such uncertainty is too large for medical applications involving patient health.

In this work, production cross sections for (p, x) reactions from all stable Mo species (^{92}Mo,$^{94-98}$Mo, ^{100}Mo) were measured using the charged particle activation method in an energy range relevant for medical isotope production. The use of isotopically enriched targets allowed cross sections leading to the formation of each technetium species to be measured independently. This knowledge is critical for estimation of technetium production for the arbitrary enrichments available for commercial medical production as well as predicting the impact from target recycling. Additionally, this comprehensive dataset in the midshell region can help constrain nuclear models.

The present paper reports the results for technetium and niobium production from a series of irradiations performed at the Nuclear Science Laboratory at the University of Notre Dame. The following section will describe the setup of the experiment as well as present a brief introduction to the nuclear reaction calculations used to guide this study. The focus of the discussion will be reserved for several previously unmeasured cross sections as well as those cross sections which display significant deviations from the theoretical calculations.

II. EXPERIMENTAL SETUP

A. Targets and irradiations

In order to isolate individual reaction channels, highly isotopically enriched targets (Microfoils, USA) were used

*elamere@mit.edu
†mcouder@nd.edu
‡Deceased.

TABLE I. Isotopic composition of enriched molybdenum targets as measured by MC-ICP-MS. The provided isotopic composition of natural abundance molybdenum from [22] is also provided.

		Target material						
Composition	Natural abundance	^{92}Mo	^{94}Mo	^{95}Mo	^{96}Mo	^{97}Mo	^{98}Mo	^{100}Mo
^{92}Mo (%)	14.5246(15)	97.51(1)	0.88(1)	0.263(3)	0.252(1)	0.217(1)	0.105(1)	0.560(3)
^{94}Mo (%)	9.1514(74)	0.701(2)	93.85(1)	0.831(2)	0.2625(6)	0.193(1)	0.0814(8)	0.186(1)
^{95}Mo (%)	15.8375(98)	0.535(1)	2.831(2)	96.184(4)	1.018(2)	0.4726(5)	0.159(2)	0.296(1)
^{96}Mo (%)	16.672(19)	0.3666(8)	1.051(1)	1.572(1)	96.24(1)	1.251(2)	0.245(2)	0.367(2)
^{97}Mo (%)	9.5991(73)	0.177(1)	0.3976(7)	0.4025(6)	1.033(3)	94.23(8)	0.361(4)	0.238(2)
^{98}Mo (%)	24.391(18)	0.414(1)	0.749(3)	0.586(2)	0.978(2)	3.326(7)	98.68(2)	0.920(5)
^{100}Mo (%)	9.824(50)	0.301(2)	0.2274(9)	0.1606(6)	0.2120(4)	0.3094(7)	0.370(4)	97.4(1)

in this study. The composition of the sample material was measured with multicollector–inductively coupled plasma mass spectrometry (MC-ICP-MS) and is provided in Table I. The thickness of each foil was determined using the energy loss of alpha particles from a mixed alpha source (^{241}Am and ^{152}Gd). A Monte Carlo calculation based on the energy loss tables from the Stopping and Range of Ions in Matter program (SRIM) [23] was used to determine the effective thickness. The targets employed in this study are in the range of 0.5–8.5 mg/cm^2. Since molybdenum is known to oxidize readily in air, the oxidation of the targets was determined postirradiation by focused ion-beam measurements on the cross-sectional surface of each foil. Due to the relatively deep sampling depth and tilted sample stage, *in situ* energy-dispersive x-ray spectroscopy was not able to determine the oxide stoichiometry with precision. However, the measurements are in agreement with an amorphous compound of 50:50 MoO_2 and MoO_3. This oxide-metal ratio was used to correct the SRIM calculation of the alpha energy loss measured for each target to obtain a corrected Mo thickness.

The targets were irradiated in a specially designed activation chamber located at the exit of the University of Notre Dame's FN tandem (10 MV) accelerator. Proton beam energies in the range of 8–19 MeV were chosen. Individual irradiations were performed in a series of runs over a several month period to allow for proper tracking of the numerous decay curves of the activated species and to allow the duration and flux to be optimized to provide consistent statistics for each produced radioisotope. Additionally, by employing a charged particle activation method with thin, single foil irradiations the proton energy resolution was optimized and straggling effects, which have been proposed by Tárkányi *et al.* [24] as a potential source of discrepancy in the cross section measurements of ^{100}Mo$(p, 2n)^{99m}$Tc, were minimized. The beam spot was focused and collimated to a well-defined circular area (<2 mm) using a pair of quadrupoles and collimators. Typical proton currents were 400–700 nA with bombardment times ranging from 5 min to 36 h. The beam intensity on target as a function of time was monitored by an electron-suppressed Faraday cup located 35 cm downstream of the target. The target irradiation station was located prior to the accelerator analyzing magnet, preventing the use of the standard electrostatic accelerator energy stabilization mechanism. Rather, the accelerator was stabilized with the generating voltmeter and the resulting proton energy profile was measured following each activation by removing the Faraday cup and sending the beam through the analyzing dipole magnet immediately downstream of the activation chamber. By varying the magnetic field in the analyzing magnet and monitoring the beam transmission, the absolute value and full width at half maximum (FWHM) of the beam energy was measured. The energy of the beam at the center of the target was calculated using the SRIM energy loss tables. The total uncertainty of the beam energy was taken as the FWHM of the incident beam added linearly to one half of the total energy loss calculated from SRIM.

B. Activity measurement

Following each irradiation, the gamma ray spectra of the activated targets were measured using a HPGe detector (depending on setup, either Canberra GC13023 or GC3518, 130% and 35% relative efficiency, respectively) which was shielded using a large Pb castle. A rigid plastic stand with a number of slots at various detector-source distances (up to 140 cm) was used to ensure reproducible measurement geometries. Energy and efficiency calibrations were performed periodically throughout the experiment at each of the fixed positions using standard sources (^{60}Co, ^{133}Ba, ^{137}Cs, ^{152}Eu, and ^{241}Am) in the energy range 60–2000 keV using 19 of the strongest gamma ray lines. Detector efficiencies for measured gamma ray lines from the activated targets were interpolated from a seventh-order polynomial fit of the logarithm of efficiency as a function of the logarithm of gamma ray energy in keV. True-coincidence summing corrections were determined using a GEANT4 [25] simulation of the detector setup. Due to the relatively large source-detector distances, these corrections were small, typically on the order of a few percent for the closest geometries employed.

No chemistry was performed on the foils prior to assaying. The cooling time between end of bombardment (EOB) and the start of counts (SOC) was generally less than 10 min, allowing short-lived isotopes (e.g., ^{92}Tc, $T_{1/2} = 4.25 \pm 15$ m) to be observed. The targets were monitored over the course of several weeks to months depending on the half-lives of the activated species. Corrections due to high count rates were applied. While the deadtime of the system was typically less than 10%, the data acquisition system was shown to be linear up to 60% deadtime using the moving source method outlined in Ref. [26]. This was particularly important for short lived isotopes where the initial deadtime was briefly observed to be up to 50%.

1. Interference corrections

The activation method is a well established technique [27] which relies on the solution to a modified set of Bateman equations. The production cross section for radioisotopes that are long-lived relative to the irradiation time can be obtained using this method by quantifying the number of atoms present at the end of bombardment through measurement of the induced activity. Proton bombardment of a molybdenum target produces a large number of radioisotopes, several of which emit overlapping energy gamma rays as a signature of their decay (see Table II). Common decay products often result in many of the most prominent gamma lines being shared, not just for produced isomers but also for several other neighboring species pairs (e.g., ^{96}Tc and ^{96}Nb, ^{95}Tc and ^{95}Nb, ^{93}Tc and ^{93m}Mo). Additionally, the decay of independent nuclei can produce gamma rays with energies which are not well separated in the detector (e.g., ^{96}Tc and ^{94}Tc, ^{95}Tc and ^{94}Tc, ^{94}Tc and ^{92}Tc and ^{89}Nb). In order to disentangle the various components of a particular gamma ray line, the count rate was tracked over many half-lives and fit with constrained exponential functions corresponding to each produced isotope. This allowed different contributions to be separated based on their isotopic origin. When possible, the consistency of the fitting procedure was investigated by comparing the evaluated activity for each species for multiple of the more intense gamma lines.

The presence of multiple decay chains with various branching ratios necessitates an extension to the simple activation formula. While more cumbersome, see Table III, the general solution to the underlying differential equation is known [31]. For this work, only decay chains with three or fewer nuclides were included. Feeding from more complicated decay pathways was not significant. The number of observed counts for a gamma line is given by the sum over all elements, i, of the decay chain,

$$C[t] = \epsilon[E] \sum_i I_i \lambda_i N[t]_i, \tag{1}$$

where $\epsilon[E]$ is the detector photopeak efficiency at energy E, I_i is the gamma intensity, λ_i is the decay constant, and $N(t)_i$ is the number of nuclei. By expanding and regrouping in terms of $e^{-\lambda_i}$, one can find, in the simple case of a two chain decay with branching,

$$\begin{aligned}\sigma_1 &= \frac{1}{\eta\Phi}\frac{D_1}{(1-e^{-\lambda_1 t_b})\left(f I_{\gamma_2}\frac{\lambda_2}{\lambda_1-\lambda_2}+I_{\gamma_1}\right)},\\ \sigma_2 &= \frac{1}{\eta\Phi}\left[\frac{D_2}{(1-e^{-\lambda_2 t_b})}\frac{1}{I_{\gamma_2}}\right.\\ &\quad\left.+\frac{D_1}{(1-e^{-\lambda_1 t_b})}\frac{f\lambda_1}{I_{\gamma_2} f\lambda_2 + I_{\gamma_1}(\lambda_2-\lambda_1)}\right],\end{aligned} \tag{2}$$

where D_1 and D_2 are the intercepts of the fitting equations at t = EOB, with $D_1 + D_2 = C$[EOB], η is the number of target atoms, Φ is the incident particle flux, and f is the branching ratio from $1 \rightarrow 2$. From Eq. (2), it is possible to extract the cross section for both radioisotopes in the decay chain simultaneously by fitting the decay curve. In practice, this

TABLE II. A summary of the nuclear data for the investigated radioisotopes observed in the γ spectrum obtained from the NNDC NuDat 2.7 database [28]. The decay product, branching ratio, half-life, and the principal γ emissions used for quantification are provided.

Product	Daughter	f (%)	Half-life	E_γ(keV)	I_γ(%)
^{101}Tc	^{101}Ru	100	14.22(1) m	306.83(3)	89(4)
^{99m}Tc	^{99}Tc	99.9963(6)	6.0072(9) h	140.511(1)	89(4)
	^{99}Ru	0.0037(6)			
^{97m}Tc	^{97}Tc	96.06(18)	91.0(6) d	96.5(1)	0.320(3)
	^{97}Mo	3.94(18)			
^{96m}Tc	^{96}Tc	98.0(5)	51.5(10) m		
	^{96}Mo	2.0(5)			
^{96}Tc	^{96}Mo	100	4.28(7) d	849.86(4)	98(4)
				778.22(4)	99.76(1)
				812.54(4)	82(3)
				1126.85(6)	15.2(12)
				434.71(5)	0.75(5)
				568.88(7)	0.92(6)
				1091.30(4)	1.10(8)
^{95m}Tc	^{95}Tc	3.88(32)	61(2) d	204.117(2)	63.2(8)
	^{95}Mo	96.12(32)		582.082(3)	30.0(4)
				786.198(4)	8.65(12)
				820.624(5)	4.71(6)
				835.149(5)	26.6(4)
^{95}Tc	^{95}Mo	100	20.0(1) h	765.789(9)	93.8(3)
				869.60(3)	0.317(8)
				1073.71(2)	3.74(4)
				204.12(1)	0.304(23)
				785.93(2)	0.145(8)
				947.67(2)	1.951(19)
^{94}Tc	^{94}Mo	100	293(1) m	871.05(7)	99.900(0)
				702.67(7)	99.6(18)
				849.74(7)	95.7(18)
				916.10(15)	7.6(4)
				449.2(3)	3.3(3)
				532.1(3)	2.35(25)
				1592.1(3)	2.25(20)
^{94m}Tc	^{94}Mo	100	52.0(10) m	871.05(7)	94.2(5)
				1522.1(2)	4.5(3)
				1868.68(8)	5.7(3)
				993.19(9)	2.21(3)
^{93}Tc	^{93}Mo	100	2.75(5) h	1362.94(7)	66.2(6)
				1477.14(8)	8.7(5)
				1520.28(9)	24.4(8)
^{93m}Tc	^{93}Tc	77.4(6)	43.5(10) m	391.83(8)	58.3(9)
	^{93}Mo	22.6(6)			
^{92}Tc	^{92}Mo	100	4.25(15) m	1509.6(3)	101(3)
				148.0(6)	71(4)
				329.3(3)	80(3)
				773.0(3)	99.857(0)
^{89m}Nb	^{89}Zr	100	66(2) m	588.0(2)	95.57(13)
^{89}Nb	^{89}Zr	100	2.03(7) h	1627.2(2)	3.5(7)
				1833.4(2)	3.3(7)
				1511.4(3)	1.9(4)
^{91m}Nb	^{91}Nb	96.6(5)	60.86(22) d	1204.67(8)	2.0(3)
	^{91}Zr	3.4(5)			
^{92m}Nb	^{92}Zr	100	10.15(2) d	934.44(10)	99.15(4)

TABLE II. (*Continued.*)

Product	Daughter	f (%)	Half-life	E_γ(keV)	I_γ(%)
^{95m}Nb	^{95}Nb	94.4(6)	3.61(3) d	235.69(2)	24.8(8)
	^{95}Mo	5.6(6)			
^{95}Nb	^{95}Mo	100	34.991(6) d	765.803(6)	99.808(7)
^{96}Nb	^{96}Mo	100	23.35(5) h	568.871(12)	58.0(3)
				778.224(15)	96.45(22)
^{97}Nb	^{97}Mo	100	72.1(7) m	657.94(9)	98.23(8)
^{91}Mo	^{91}Nb	100	15.49(1) m	1637.3(1)	0.329(21)
				1581.5(1)	0.226(14)
^{93m}Mo	^{93}Mo	99.88(1)	6.85(7) h	1477.138(3)	99.1(11)
	^{93}Nb	0.12(1)		684.693(21)	99.9(8)
				263.049(13)	57.4(11)
^{99}Mo	^{99}Tc	12.27	65.924(6) h	140.511(1)	5.1(2)[a]
	^{99m}Tc	87.73		181.068(8)	6.05(12)
				739.500(17)	12.20(16)

[a]This value refers to the gamma intensity of ^{99}Mo directly rather than the gamma intensity of the 140.5 keV line in equilibrium with ^{99m}Tc. This value is taken from [29]. Other authors have used a slightly lower value from Be *et al.* [30]. The impact of this change on the ^{99m}Tc production cross section in this proton energy range is minor.

expression was modified to include contributions from open reaction channels on trace Mo contamination in the target. This was accomplished by solving the differential equations in Table III with additional production terms.

The need to separate contributions from decay chains has been addressed explicitly in several recent works [11,24,29,32–34] specifically for the ^{99}Mo→^{99m}Tc decay chain. This treatment of the growth/decay is a generalization applicable for all the cases in this work. From the solutions provided in Eq. (2), it is possible to express a cumulative cross section for a long-lived daughter,

$$\sigma_2^{\text{eff}} = \sigma_2 + \frac{f\lambda_1}{\lambda_1 - \lambda_2}\sigma_1, \tag{3}$$

where σ_2^{eff} is the effective cross section for the production of the daughter isotope following the decay of the feeding isotope. Equation (3) was used to provide calculated cumulative cross sections for comparison to published experimental data in the results section.

It has been suggested that many of the earlier works measuring ^{100}Mo(p, $2n$)^{99m}Tc inadvertently reported the effective cross section, from direct production and decay into ^{99m}Tc [12]. Such an explanation could possibly account for the discrepancies at higher proton energy ($E_p > 20$ MeV), where the ^{100}Mo(p, pn)^{99}Mo cross section becomes large. The scatter in literature values below 13 MeV where the cross section for ^{100}Mo(p, pn)^{99}Mo is relatively small remains not well understood.

2. Uncertainties

The activity of each isotope was measured using between one and eight independent gamma ray lines. A weighted sum for each isotope was used to determine the EOB activity. The correlation of the fitting parameters for the decay curves was taken into account when determining the uncertainty in the EOB activity. The typical uncertainty associated with the intercept from the decay curve fitting was 1–10%. To determine the total uncertainty in the cross section, this uncertainty in the activity was added in quadrature to the uncertainty from the HPGe calibration (2–4%), the summing corrections (<1%), and the nuclear data (typically 2–5%). Additionally, the uncertainty in the target thickness from the MC SRIM calculation and fitting (10%), the target composition from MC-ICP-MS measurements (<0.5%), the oxide corrections from focused ion beam measurements (10%), and the proton flux calibration (1%) were added linearly to the statistical cross section uncertainty. An overview of typical uncertainties is provided in Table IV.

C. Nuclear model calculations

In the energy and mass range considered in this work, cross sections were evaluated using a statistical formalism for nuclear reactions, developed by Wolfenstein, Hauser, and Feshbach [35,36]. This framework relies on the choice of numerous underlying theoretical models for various nuclear physics inputs. Several nuclear reaction codes exist, the most prevalent in medical isotope production studies are EMPIRE [37] and TALYS [38,39], which are meant to be general, flexible, and straightforward tools for researchers. Both codes allow the choice of nuclear input models to be varied while

TABLE III. The differential equations governing the production and decay of the produced radioisotopes of a two member decay chain (1 → 2) are provided. The solution to these equations, found in a similar form in Ref. [12], represents a simplified case of a more general class of problems [31]. In these equations, N is the number of nuclei, R is the production rate during bombardment, assumed constant ($R = \sigma\eta\Phi$), and t_b is the duration of bombardment. Note that the solution is valid only for $t > t_b$.

Differential equation	Solution (for $t > t_b$)
$dN_1 = \begin{cases} (R_1 - \lambda_1 N_1)dt & : 0 < t < t_b \\ -\lambda_1 N_1 dt & : t_b < t \end{cases}$	$N_1[t] = \frac{R_1(1 - e^{-\lambda_1 t_b})e^{-\lambda_1(t-t_b)}}{\lambda_1}$
$dN_2 = \begin{cases} (R_2 - \lambda_2 N_2 + f\lambda_1 N_1)dt & : 0 < t < t_b \\ (-\lambda_2 N_2 + f\lambda_1 N_1)dt & : t_b < t \end{cases}$	$N_2[t] = (1/\lambda_2)(R_2 + f\frac{\lambda_1}{\lambda_1-\lambda_2}R_1)(1 - e^{-\lambda_2 t_b})e^{-\lambda_2(t-t_b)}$ $- \frac{f}{\lambda_1-\lambda_2}R_1(1 - e^{-\lambda_1 t_b})e^{-\lambda_1(t-t_b)}$
with Initial Conditions : $N_1(0) = N_2(0) = 0$	

TABLE IV. Typical uncertainty values (%) considered in the cross section calculation.

	Typical uncertainty (%)
Decay curve fitting	1–10
HPGe efficiency calibration	2–4
Summing corrections	<1
Nuclear data	2–5
Target thickness	10
Target composition	<0.5
Oxide correction	10
Proton flux calibration	1
Total	∼15–25

also incorporating contributions from pre-equilibrium and direct reactions.

Such attributes make these codes useful for investigating the feasibility of producing medical quantities of ^{99m}Tc through proton bombardment. EMPIRE has been used to calculate yields of coproduced radionuclidic impurities using natural abundance and enriched ^{100}Mo targets [40]. These calculations are being used to optimize irradiation conditions (duration, current, target composition and thickness, and incident energy) to quantify and minimize patient dose increase. However, as Celler *et al.* [40] discuss, experimental cross section measurements are critical to feasibility studies of ^{99m}Tc production as different nuclear model inputs can produce significant variation in statistical model predicted cross sections.

One of the goals of the nuclear calculation section of this work is to investigate how well the default parameters used in such reaction codes reproduce our experimental data as well as other data available in the literature. Additionally, by varying the model input choice, the theoretical variation in cross section in this mass region can be investigated.

Calculations were performed using the nuclear model code TALYS 1.8. An example input file is provided in the Supplemental Material [41]. Independent variation of all the available parameters in TALYS is outside the scope of this study. To limit the number of calculations performed, the parameters significantly impacting the cross section estimate were varied in TALYS (i.e., the choice of level density, optical model potential, γ strength function, and deformation parameter). This variation was used to estimate the uncertainty that model choice has on cross section calculations. The first and third quartile (corresponding to the gray band in the cross section plots) as well as the maximum and minimum values (dashed lines) for each energy point are plotted with the experimental measurements. Calculations which combined phenomenological and semimicroscopic models were excluded. Additionally, the results of the default TALYS calculations (black, solid line) are provided.[1]

[1]Note that the default calculation does not represent a median value in the TALYS calculation band and occasionally [e.g., ^{97}Mo$(p, n)^{97m}$Tc] defines the extreme in certain energy ranges.

III. RESULTS AND DISCUSSION

The irradiation of molybdenum targets with a ∼20 MeV proton beam results in the production of various technetium, molybdenum, and niobium species through (p, γ), (p, xn), (p, pn), (p, α), and $(p, n\alpha)$ reaction channels. For each molybdenum target, we report on cross sections larger than >0.5 mb whenever possible. Additionally, an effort was made to measure the production cross section of isomeric and ground states independently. These results are summarized in Table V. Cumulative cross sections are provided when this separation was not possible, for instance when the metastable state is short lived or has weak intensity (e.g., $^{96(m+g)}$Tc) or when multiple production pathways are open on the same target [e.g., ^{100}Mo$(p, pn)^{99}$Mo and ^{100}Mo$(p, 2p)^{99}$Nb→^{99}Mo].

For the sake of brevity, only cross section measurements which show disagreement with previous literature or for which no previous literature exists will be discussed in detail. The measurements for ^{100}Mo$(p, 2n)^{99m}$Tc and ^{100}Mo$(p, pn)^{99}$Mo, despite being well measured previously, are included due to their importance for medical isotope production. The cross sections for this subset of the data are plotted in Figs. 1–9, along with TALYS calculations, and previous measurements for comparison. A comprehensive set of figures for all our results is provided in the Supplemental Material [41]. In the discussion section, the default TALYS cross section will be used for comparison with the data from this work. As discussed by Takács *et al.* [42], the adopted cross section for the ^{nat}Mo $(p, x)^{96(m+g)}$Tc used by Levkovski as a monitor reaction has to be revised. Therefore, in all the figures a scaling factor of 0.75 has been applied to the results of Levkovski as suggested by [12] for this reaction. Additionally, reported data sets from natural abundance targets have been scaled, when appropriate, based on the isotopic composition from Table I for direct comparison with this work. These data sets are marked with a asterisks (∗) in the figure legend. The first author's surname and final two digits of the year of publication for each data set are provided in the legend for cross reference between figures.

A. Technetium production

The measurement of cross sections for technetium production through (p, xn) reactions was the primary objective of this work. In total, 20 individual Tc excitation curves were measured that, to a large degree, agree with available literature. However, five reactions, ^{92}Mo$(p, n)^{92}$Tc, ^{92}Mo$(p, \gamma)^{93m,g}$Tc, ^{97}Mo$(p, n)^{97m}$Tc, and ^{98}Mo$(p, 2n)^{97m}$Tc, had not previously been measured.

1. ^{92}Mo$(p, n)^{92}$Tc *reaction*

The activity of ^{92}Tc, produced exclusively from ^{92}Mo(p, n), was determined from four gamma decay lines (148.0, 329.3, 773.0, and 1509.6 keV). While displaying a very similar trend to the TALYS calculations, our measurements suggest that TALYS underpredicts this cross section by 30% (see Fig. 1). Despite this larger than anticipated cross section, ^{92}Tc will not constitute a significant concern as a radiocontaminant in ^{99m}Tc production from proton irradiation due to its short half-life and stable decay product.

TABLE V. Measured cross section data for the formation of Tc, Mo, and Nb radionuclides.[a]

Reactant	Proton energy (MeV)	Cross section (mb) for product						
^{92}Mo		^{89m}Nb	^{89}Nb	$^{91(m+g)}$Mo	^{91m}Nb ^{cum}	^{92}Tc	^{93m}Tc	^{93}Tc
	10.52(6)	0.106(15)	0.17(4)			233(33)	1.77 (26)	3.4 (5)
	13.03(6)	1.07(16)	1.6(4)		0.82(22)	483(72)	0.55(8)	1.42(22)
	15.07(2)	2.5(5)	4.3(12)		10.4(29)	550(110)	0.56(12)	1.09(24)
	16.07(2)	3.3(6)	6.2(17)	28(11)	20(6)	467(90)	0.57(13)	1.04(21)
	17.05(4)	4.3(7)	8.4(21)	143(29)	40(10)	457(73)	0.45(11)	0.98(20)
	18.07(2)	5(1)	11(3)	246(54)	67(19)	331(65)	0.50(13)	1.13(26)
^{94}Mo		^{91m}Nb	^{93m}Mo	^{93m}Tc	^{93}Tc	^{94m}Tc	^{94}Tc	
	9.04(4)					345(72)	74(15)	
	10.06(4)	3.4(9)				445(63)	97(14)	
	11.05(4)	5.1(14)				469(66)	123(17)	
	12.05(4)	4.9(13)				481(70)	145(21)	
	13.04(5)	4.3(12)				465(89)	172(33)	
	14.04(5)	5.6(16)			7.7(15)	363(70)	156(30)	
	15.04(5)	4.2(11)		20(3)	134(20)	262(39)	128(19)	
	16.06(4)	4.9(15)	0.12(3)	65(14)	292(65)	175(39)	105(23)	
	17.06(3)	6.0(16)	0.21(4)	111(18)	457(76)	118(20)	73(12)	
	18.05(4)	4.8(16)	0.48(13)	103(27)	391(102)	59(15)	36(10)	
	19.06(3)	5.3(17)	0.85(21)	121(30)	467(116)	45(11)	26(7)	
^{95}Mo		^{91m}Nb	^{92m}Nb	^{94m}Tc	^{94}Tc	^{95m}Tc	^{95}Tc	
	10.57(2)		2.0(5)			160(40)	373(92)	
	12.01(8)		3.3(6)			159(31)	412(81)	
	13.02(7)	0.07(4)	4.5(10)	21(5)	15(3)	154(34)	436(97)	
	14.03(6)	0.27(12)	5.2(7)	150(21)	107(15)	100(14)	306(42)	
	15.07(2)		4.5(10)	236(50)	179(38)	59(13)	181(39)	
	16.03(6)	1.1(3)	5.1(10)	326(66)	238(48)	35(7)	118(24)	
	17.99(6)	3.4(10)	3.5(7)	385(76)	324(64)	16(3)	50(10)	
	19.03(6)	3.9(13)	2.8(6)	420(93)	310(69)	11.1(25)	35(8)	
^{96}Mo		^{92m}Nb	^{95m}Tc	^{95}Tc	$^{96(m+g)}$Tc			
	8.04(5)				489(68)			
	10.06(3)				767(126)			
	11.07(3)				778(187)			
	11.55(4)				700(113)			
	12.07(3)		8(2)	61(17)	652(160)			
	12.55(4)		43(6)	94(13)	714(104)			
	13.06(3)		86(12)	176(25)	543(80)			
	14.05(4)	0.18(7)	190(36)	379(72)	399(76)			
	15.05(3)	0.25(6)	250(59)	506(119)	244(57)			
	16.05(4)	0.71(12)	273(45)	580(97)	149(25)			
	17.05(4)	1.95(29)	270(40)	605(91)	97(15)			
	18.05(4)	4.3(6)	285(39)	683(94)	74(10)			
	19.06(3)	7.1(11)	281(45)	721(116)	61(10)			
^{97}Mo		$^{96(m+g)}$Tc	^{97m}Tc					
	9.01(8)		134(29)					
	10.05(4)		156(34)					
	10.98(11)	13.0(30)	160(33)					
	11.98(10)	238(51)	110(28)					
	13.02(6)	473(73)	67(15)					
	14.02(6)	690(110)	43(10)					
	15.04(6)	769(125)	27(6)					

TABLE V. *(Continued.)*

Reactant	Proton energy (MeV)	Cross section (mb) for product				
^{98}Mo		^{95m}Nb	^{95}Nb	^{97m}Tc	^{99m}Tc	
	10.06(3)	1.01(15)	0.63(10)	6.4(15)	0.33(10)	
	11.06(3)	1.23(21)	0.90(18)	71(15)	0.13(9)	
	12.05(4)	1.9(4)	1.6(3)	158(36)	0.25(12)	
	13.06(3)	2.0(3)	2.6(4)	209(44)	0.17(11)	
	14.05(3)	2.8(4)	3.5(6)	256(52)	0.33(13)	
	15.05(3)	2.9(4)	5.4(8)	290(60)	0.35(13)	
	16.06(3)	3.0(5)	5.2(9)	268(56)	0.33(13)	
	17.06(3)	2.6(4)	5.1(8)	262(54)	0.22(11)	
	18.02(2)	2.0(5)	4.1(10)	202(54)	0.15(9)	
	19.05(4)	1.80(29)	4.5(7)	213(45)	0.24(9)	
^{100}Mo		^{96}Nb	$^{97(m+g)}$Nb	^{99}Mo	^{99m}Tc	^{101}Tc
	8.01(8)		0.19(3)	0.0033(11)	0.35(5)	0.43(7)
	9.01(7)		0.53(7)	0.035(5)	67(9)	0.45(7)
	10.07(2)		1.05(22)	1.5(3)	145(31)	0.53(12)
	11.01(7)		1.80(29)	1.29(21)	195(31)	0.54(10)
	12.02(6)		2.6(4)	4.7(6)	224(30)	0.55(9)
	13.03(6)		3.6(5)	11.9(17)	254(37)	0.63(10)
	14.03(2)	0.23(3)	4.2(6)	21(3)	249(35)	0.60(10)
	15.07(2)	0.59(16)	4.3(12)	33(9)	239(64)	0.60(17)
	16.04(5)	1.38(19)	4.6(6)	48(7)	240(34)	0.48(8)
	17.03(5)	2.6(4)	4.7(7)	64(9)	241(34)	0.45(7)
	18.07(2)	3.7(9)	4.3(11)	79(19)	228(56)	0.44(11)
	19.07(2)	5.8(12)	4.5(10)	103(22)	226(48)	0.54(14)

[a]Note that cumulative cross sections are marked with "cum" in superscript for isotopes which have contributions from short-lived decay products. Isotopes that are fed directly by their isomer (which was not measured) are marked "(m + g)".

2. ^{92}Mo$(p, \gamma)^{93m,g}$Tc *reactions*

The short lived, 43.5 m, isomer ^{93m}Tc has a large branching, 77.4%, to the coproduced isotope ^{93g}Tc. The activity of ^{93m}Tc was primarily determined from the intense, independent gamma ray line of the isomeric transition at 391 keV. In the ^{92}Mo$(p, \gamma)^{93m}$Tc reaction, the isomer's activity was also confirmed for $E_p \leqslant 16$ MeV by measurement of the grow-in of ^{93g}Tc from its intense 1392 keV gamma line. The activity of ^{93g}Tc was determined from three lines: 1392, 1477, and 1520 keV.

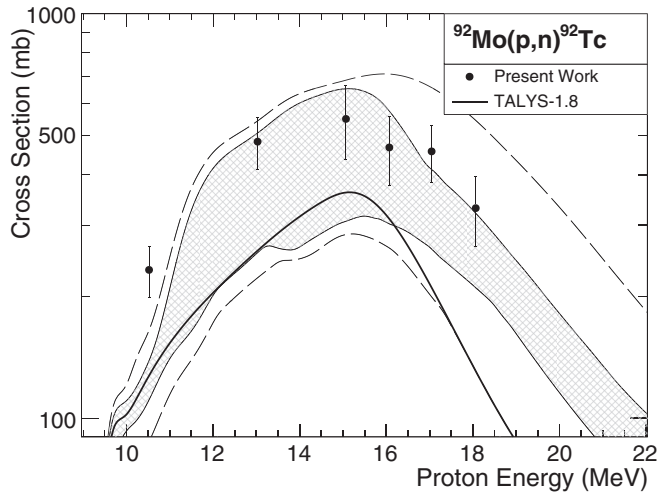

FIG. 1. Comparison of measured reaction cross sections of ^{92}Mo$(p, 2n)^{92}$Tc to the default TALYS predictions, shown with the black, solid line. Variation of several model parameters were explored in this work (see Sec. II C). The maximum and minimum results are shown with dashed lines as well as the first and third quartile values represented by the gray band.

Since ^{93}Mo is not stable, the production of ^{93}Tc in the experimental energy range comes from just two reaction channels: ^{92}Mo(p, γ) and ^{94}Mo$(p, 2n)$. Our cross section measurements are presented in Figs. 2(a) and 2(b) along with the various investigated TALYS calculations. While there is no literature for cross sections in this work's energy range measured on isotopically enriched ^{92}Mo targets, measurements on natural abundance targets at energies below the threshold for the ^{94}Mo$(p, 2n)^{93m,g}$Tc reactions (13.8 and 14.2, respectively) yield cross sections that can be scaled to compare directly with our measurements (see Fig. 2). Below 14 MeV, our measurements show reasonable agreement with [24,32,33] and suggest that TALYS models underpredict ^{93}Tc production for both the ground state and isomer.

3. ^{97}Mo$(p, n)^{97m}$Tc *and* ^{98}Mo$(p, 2n)^{97m}$Tc *reactions*

The cross section for ^{97m}Tc production from a natural abundance target was recently reported by Červenák and Lebeda [32]. Below ~24 MeV, the production of ^{97m}Tc in a natural abundance target results from (p, n) and $(p, 2n)$

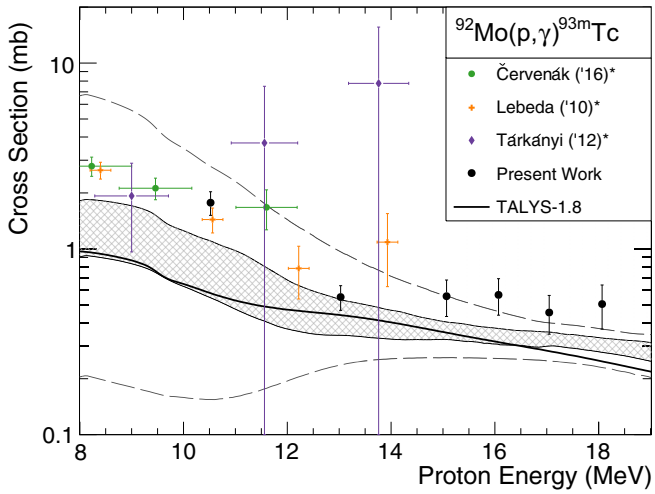

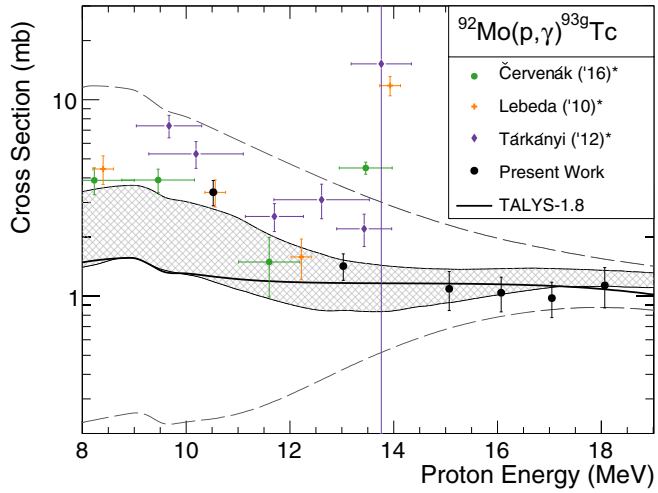

FIG. 2. Comparison of measured reaction cross sections of ^{92}Mo(p, γ)^{93}Tc to TALYS calculations (see Fig. 1 for description). The data are from this work and from [24,32,33]. Equation (3) was used to calculate the values of ^{92}Mo(p, γ)^{93g}Tc for [33].

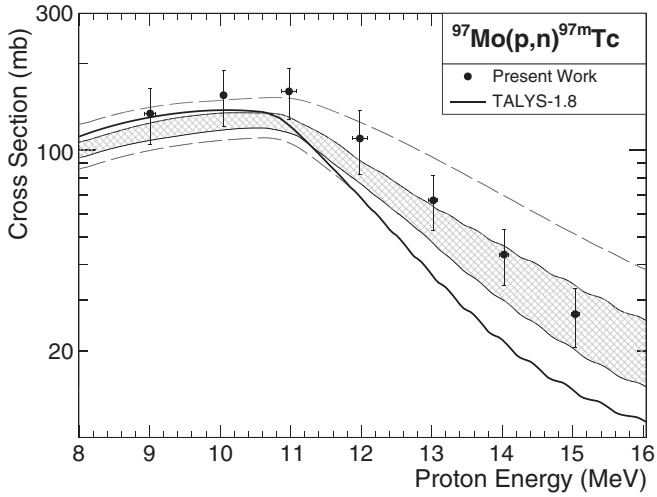

FIG. 3. Comparison of measured reaction cross sections of ^{97}Mo(p, n)^{97m}Tc to TALYS calculations (see Fig. 1 for description).

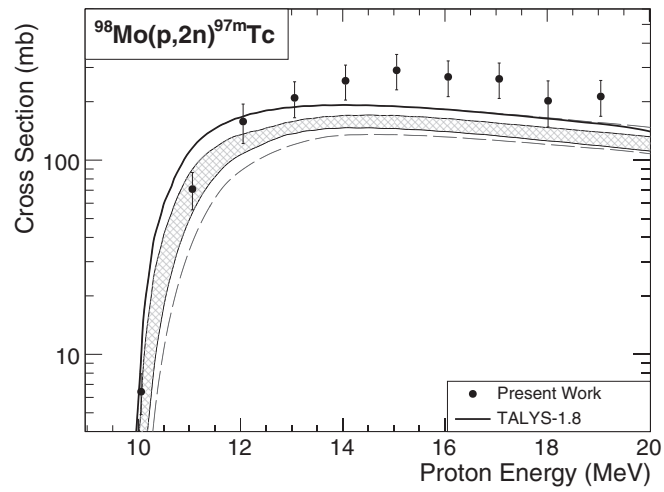

FIG. 4. Comparison of measured reaction cross sections of ^{98}Mo(p, $2n$)^{97m}Tc to TALYS calculations (see Fig. 1 for description).

reactions on ^{97}Mo and ^{98}Mo, respectively. With the exception of a small proton energy range between 14 and 17 MeV, where we report a roughly 30% higher value, our results scaled for natural abundance support this earlier work. Importantly, however, we are able to separate the two contributions. Our results show that theoretical models reproduce the shape of the excitation curve for ^{97}Mo(p, n), but underpredict the amplitude by roughly 20% (see Fig. 3). For ^{98}Mo(p, $2n$)^{97m}Tc the agreement is worse, with a qualitatively different shape and an underprediction of the magnitude of the cross section above 13 MeV by nearly 70% (see Fig. 4). Since ^{98}Mo is the closest stable molybdenum isotope in mass to ^{100}Mo, and has the highest natural abundance, it will be the primary contaminant in an enriched ^{100}Mo target. Therefore, understanding the production of radionuclidic impurities from ^{98}Mo(p, xn) is critical for determination of the feasibility of cyclotron produced ^{99m}Tc. Such deviations from statistical model calculations could significantly impact dose increase calculations. Uncertainty in the production of ^{97m}Tc is of particular concern as the quality control test for the radionuclidic purity of cyclotron-produced ^{99m}Tc proposed by Tanguay *et al.* [43] will be insensitive to this contaminant due to its low energy (96 keV) gamma ray.

4. ^{100}Mo(p, $2n$)^{99m}Tc *reaction*

The majority of literature available on the production of technetium through proton bombardment reactions, (p, xn), concerns ^{99m}Tc at medical cyclotron energies (10–24 MeV). As ^{99}Mo is unstable and the cross section of ^{98}Mo(p, γ) is minimal (<0.5 mb), ^{99m}Tc production stems mainly from just one channel, allowing results from natural abundance targets to be extended to ^{100}Mo(p, $2n$).

The activity of ^{99m}Tc was measured from the 140.5-keV gamma ray line, which required removing the contribution of ^{99}Mo and also the small (p, γ) contribution from contaminant ^{98}Mo in the target. At higher proton energies, attention must also be paid to the interfering gamma ray at 141.18 keV of ^{90}Nb produced primarily (at energies below 28 MeV) by

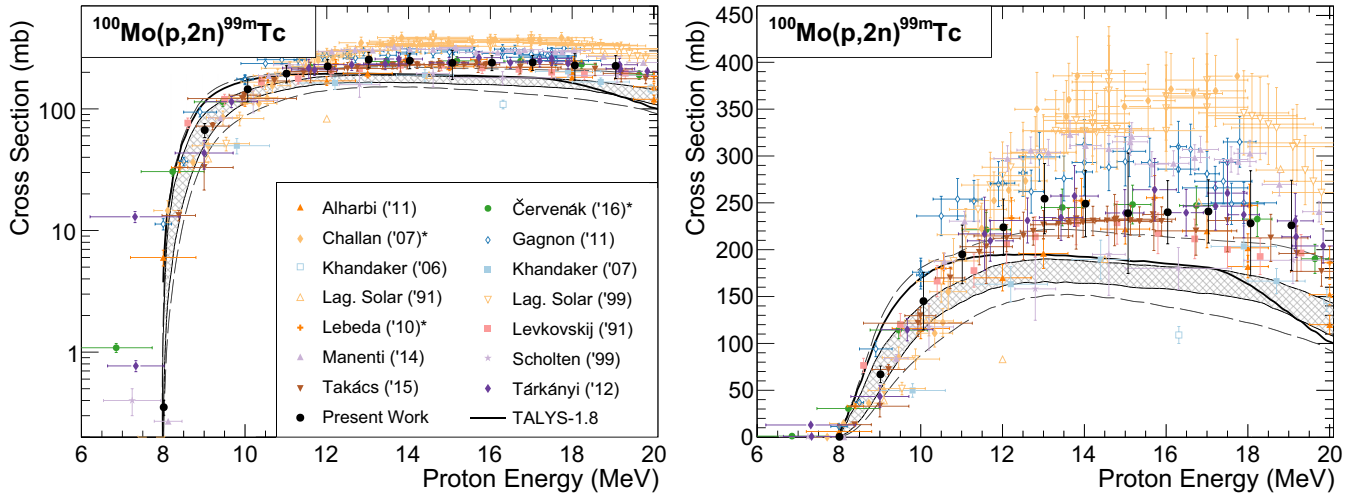

FIG. 5. Comparison of measured reaction cross sections of ^{100}Mo(p, $2n$)^{99m}Tc to TALYS calculations (see Fig. 1 for description) shown in both logarithmic (left) and linear scale (right). The data are from this work and from [8,9,11,24,29,32–34,44–49]. Note that (1) the data of Takács *et al.* [34] include their reevaluated values from Takács *et al.* [50]; (2) the measurements of Lagunas-Solar have not been corrected for production of ^{90}Nb in the natural abundance target. Below 20 MeV, however, the cross section for production, primarily ^{94}Mo(p, $n\alpha$)^{90}Nb, is negligible.

reactions on ^{94}Mo, although channels from ^{92}Mo and ^{95}Mo are also open. Due to the high enrichment of the ^{100}Mo target and incident energies below 20 MeV, this correction was insignificant.

The results from this work are displayed in Fig. 5 together with numerous previous measurements and the TALYS calculations. There appears to be a large amount of scatter in the published values, especially above 11 MeV, the source of which is uncertain. Several suggestions exist in the literature regarding possible causes, with the most promising explanation being the improper treatment of grow-in from coproduced ^{99}Mo as mentioned previously. However, it appears that more than one issue may be involved as the cross section of ^{100}Mo(p, pn)^{99}Mo below 12 MeV is <5 mb and from Fig. 5 it is clear that the literature data sets diverge significantly below this energy.

Our data support the work of [16,24,32,34] and the reevaluated work of [50], which collectively suggest an intermediate-to-low value for the cross section up to 19 MeV. The data from [8,11,29,45,48,49] are higher, with the measurements of [8] having the worst agreement with other data sets. Conversely, the measurements of [9,46,47], and to some extent—although there is moderate scatter—[44], suggest a lower cross section. Our results, along with nearly all other data sets, disagree with the TALYS results, which underpredict the cross section above 10 MeV. This discrepancy is highly consequential for feasibility studies that rely on nuclear models as variation in this cross section directly impacts the expected radionuclidic purity.

B. Molybdenum production

Production of Mo both directly and indirectly [e.g., ^{95}Mo(p, $2n$)^{94}Tc→^{94}Mo] will cause evolution of the target's isotopic composition, a factor known to significantly impact the efficacy and non-^{99m}Tc patient dose in produced radiopharmaceuticals [18,40]. While the present experimental method does not allow for the measurements of cross sections leading to stable isotopes, the cross section measurements of the unstable Mo species, ^{91mg}Mo, ^{93m}Mo, and ^{99}Mo, may help guide more accurate statistical model predictions for reactions producing stable Mo. Together with our measurements, these model constraints will allow more accurate determination of the evolution of the target's composition after multiple reprocessing cycles.

1. ^{92}Mo(p, $2n$)$^{91(m+g)}$Mo *reaction*

The ground state of ^{91}Mo is produced both directly via ^{92}Mo(p, pn)^{91g}Mo and also through the production and decay of its short-lived (65.0 s) isomer, ^{91m}Mo. Since the isomer's lifetime is too short to measure with the activation setup

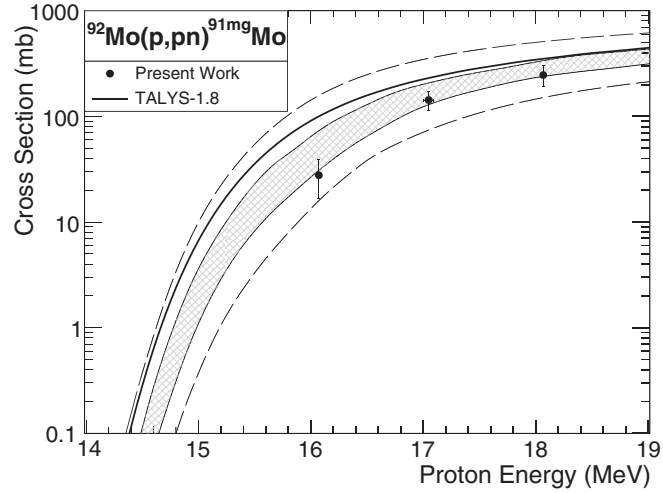

FIG. 6. Comparison of measured reaction cross sections of ^{92}Mo(p, pn)$^{91(m+g)}$Mo to TALYS calculations (see Fig. 1 for description). The data are from this work and from [24,32,46].

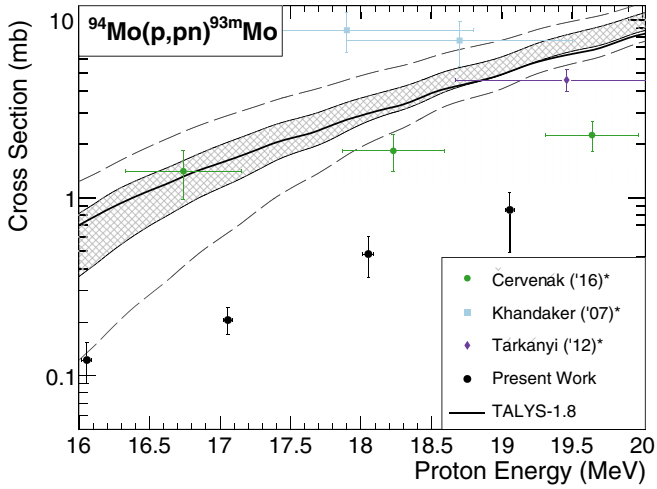

FIG. 7. Comparison of measured reaction cross sections of ^{94}Mo(p, pn)^{93m}Mo to TALYS calculations (see Fig. 1 for description). The data are from this work and from [24,32,46].

used in this work, a cumulative cross section is reported. The activity of ^{91g}Mo was quantified from its most intense gamma ray line at 1637.3 keV ($I_\gamma = 0.329\%$) after allowing sufficient time for ^{91m}Mo to decay completely. To our knowledge, this is the first cross section measurement for this reaction. The results, shown in Fig. 6, show good agreement with the TALYS calculated values.

2. ^{94}Mo(p, $2n$)^{93m}Mo *reaction*

The activity of ^{93m}Mo was determined from its 1477-, 684-, and 263-keV peaks. While it can be produced by both ^{94}Mo(p, pn) and ^{95}Mo(p, $p2n$), the (p, $p2n$) reaction threshold was too high (∼19 MeV) to be observed during this experiment. As shown in Fig. 7, there is a large spread in the reported data for this reaction. Early measurements from Khandaker *et al.* [46] appear too large at $E_p \leqslant 19$ MeV. Tárkányi *et al.* [24] have three data points between 19 and 24 MeV which seem to display some scatter making the trend difficult to determine. The most recent paper from Červenák and Lebeda [32] report a moderately larger (2×) cross section. While significantly lower than the rest of the measured work, our points have smaller statistical error bars on this weak reaction due to the use of an enriched target.

3. ^{100}Mo(p, pn)^{99}Mo *reaction*

At proton beam energies higher than $E_p > 12$ MeV ^{99}Mo is produced from ^{100}Mo directly through ^{100}Mo(p, pn)^{99}Mo and indirectly through the decay of ^{99}Nb, (i.e., ^{100}Mo(p, $2p$)^{99}Nb $\rightarrow$ ^{99}Mo). Since the half-lives of ^{99m}Nb and ^{99g}Nb are just 15 s and 2.6 m, respectively, papers typically report a cumulative cross section for the production of ^{99}Mo. Since our maximal energy is above the threshold for ^{100}Mo(p, $2p$)^{99}Nb of 11.3 MeV, but below the energy where the reaction becomes appreciable (∼24 MeV), the reported cross sections have virtually no contribution from ^{99}Nb, but can still be considered a cumulative cross section.

The activity of ^{99}Mo was determined from the independent gamma ray lines at 181 and 739 keV, as well as 140 keV, which is shared with the decay of ^{99m}Tc. Our cross section measurements for ^{100}Mo(p, pn)^{99}Mo, as well as the literature values, are shown in Fig. 8. The general trend of all measurements agree with TALYS, but are shifted down in energy by roughly 2 MeV. The exceptions are the two measurements by Lagunas-Solar et al. [8,48], which are scattered at much lower cross section values. Our measurements agree well with the measurements of Červenák and Lebeda [32], Alharbi *et al.* [44], and the reevaluated 2003 and 2015 measurements of Takács *et al.* [34]. Good agreement with our results can also be found after excluding a few unusual points (the two lowest energy points of Khandaker *et al.* [46] which appear high, and the low values of Tárkányi *et al.* [24] and Scholten *et al.* [9] at $E_p \geqslant 18$ MeV). Relative to our measurements, the excitation curves of Levkovskij [49], Lebeda *et al.* [33], Zhao *et al.* [52], Gagnon *et al.* [11], and Manenti *et al.* [29] all appear to be slightly too high.

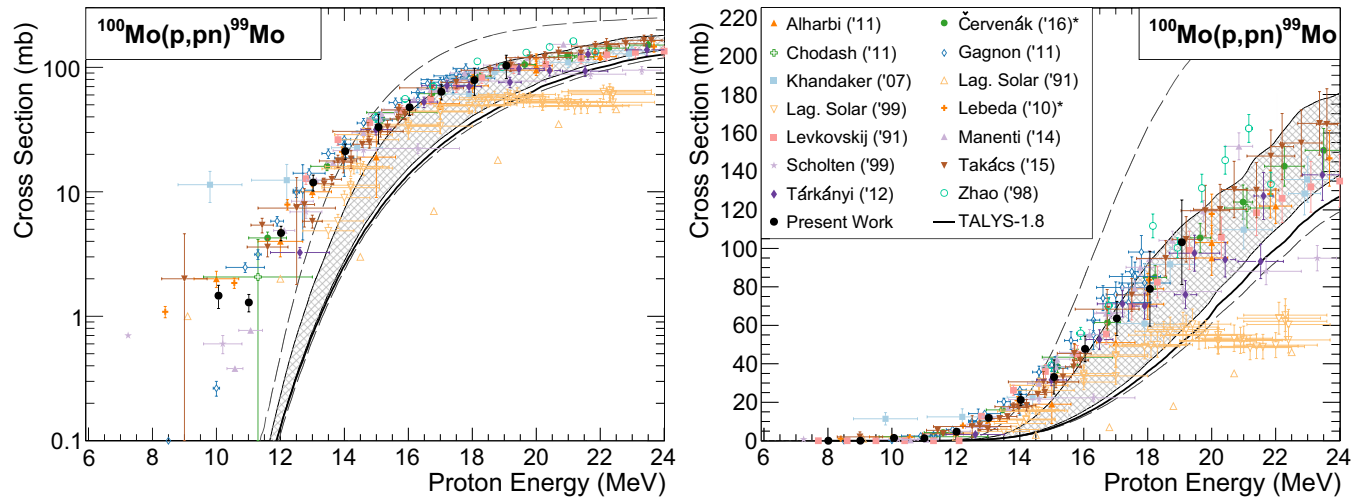

FIG. 8. Comparison of measured reaction cross sections of ^{100}Mo(p, pn)^{99}Mo to TALYS calculations (see Fig. 1 for description) shown in both logarithmic (left) and linear scale (right). The data are from this work and from [8,9,11,24,29,32–34,44,46,48,49,51,52].

At energies above 19 MeV, which were not experimentally measured in this work, the default TALYS parameters continue to underpredict the ^{100}Mo$(p, pn)^{99}$Mo cross section relative to the majority of experimental values. Above 22 MeV, the published experimental values show increased scatter and a direct comparison to TALYS or the TALYS-based evaluated nuclear data library (TENDL) is more difficult to make [32,53].

C. Niobium production

While not the primary focus of the work, eight cross sections for Nb production through $(p, 2pxn)$ were measured in this study. Our measurements of ^{92}Mo$(p, \alpha)^{89m,g}$Nb, ^{95}Mo$(p, \alpha)^{92m}$Nb, ^{96}Mo$(p, n\alpha)^{92m}$Nb, ^{98}Mo$(p, \alpha)^{95m,g}$Nb, ^{100}Mo$(p, n\alpha)^{96m}$Nb, and ^{100}Mo$(p, x)^{97(m+g)}$Nb mostly agree with the results of previous studies [32,49,54] and so will not be discussed. However, cross section measurements of ^{92}Mo$(p, x)^{91m}$Nb ^{cum}, ^{94}Mo$(p, \alpha)^{91m}$Nb, and ^{95}Mo$(p, n\alpha)^{91m}$Nb have not previously been reported. These results are discussed below.

^{92}Mo, ^{94}Mo, *and* ^{95}Mo$(p, x)^{91}$Nb *reactions*

The activity of ^{91m}Nb was determined through the independent gamma ray line at 1204 keV. The large number of reaction pathways leading to the production of ^{91m}Nb combined with the low overall cross section, weak gamma ray intensities, and long half-life make accurate cross section measurements difficult. The literature values that are available for the natural abundance cross section [24,32] display large uncertainties and significant scatter. In addition, it is not possible to disentangle contributions of the various open channels feeding ^{91m}Nb and therefore the results of those measurements are not displayed in Fig. 9. The cross section reported in Fig. 9(a) represents the cumulative cross section through ^{91m2}Nb (3.76 μs), ^{91g}Mo (15.49 m), and ^{91m}Mo (64.6 s). Above $E_p = 19.9$ MeV, the production of ^{91g}Tc and ^{91m}Tc from ^{92}Mo$(p, 2n)$, which decay into ^{91g}Mo and ^{91m}Mo, further complicates the cumulative production of ^{91m}Nb. Since this work was restricted to energies less than 19 MeV, this feeding decay did not need to be considered in our study, but may contribute to the scatter seen in the available literature at higher energies. The cross sections for ^{91m}Nb production from ^{94}Mo and ^{95}Mo, shown in Figs. 9(b) and 9(c), can be treated directly as there is no contribution from the production of ^{91}Mo.

The general trend of the excitation curve for ^{92}Mo$(p, 2p)$ shown in Fig. 9(a) appears consistent with the TALYS prediction for ^{92}Mo$(p, x)^{91}$Nb, however, the ^{94}Mo(p, α) data plotted in Fig. 9(b) display significant scatter and do not seem to follow the positively sloped TALYS curve. The reason for this disparity is not clear, however, other authors have reported only partial success reproducing $(p, n\alpha)$ cross sections with TALYS in this mass range [12]. The results for ^{95}Mo$(p, n\alpha)^{91}$Nb, shown in Fig. 9(c), have an overall trend that is similar to the TALYS estimate but don't present the local maximum at ~13 MeV calculated by TALYS.

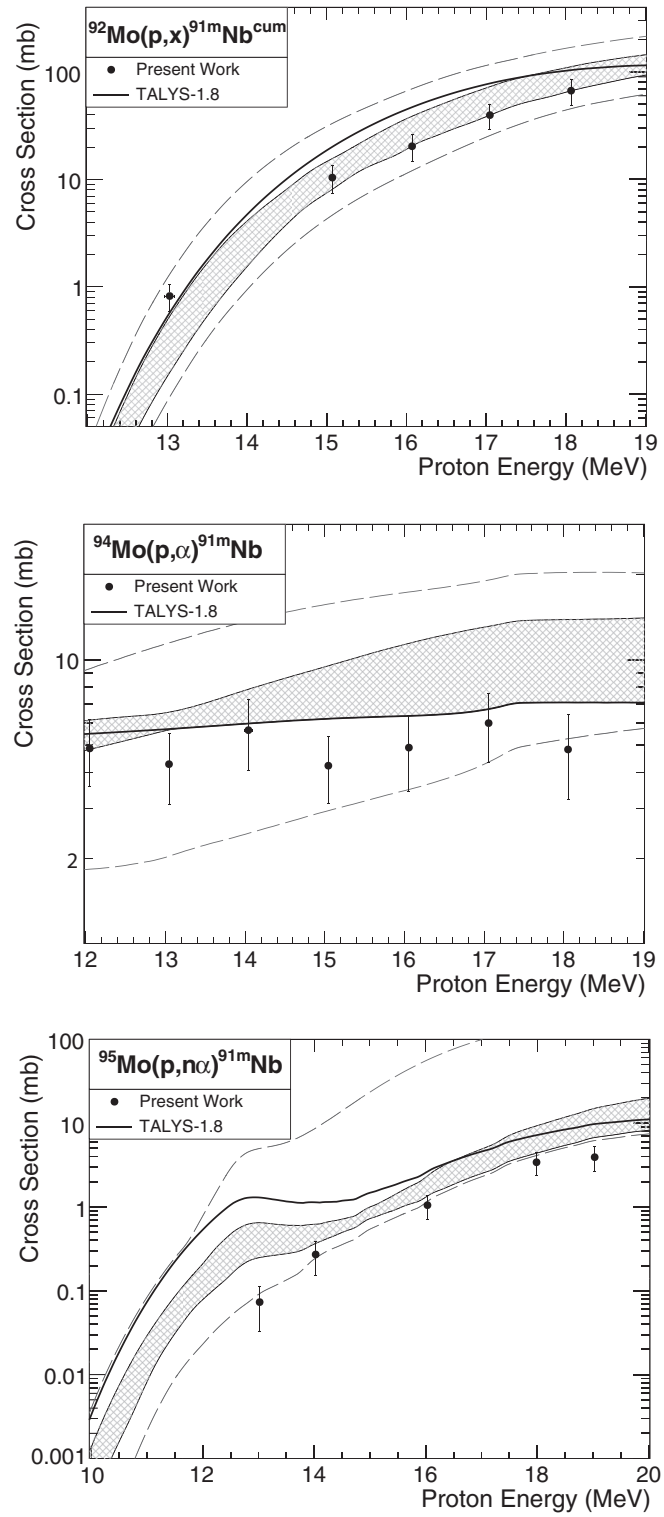

FIG. 9. Comparison of measured reaction cross sections for proton induced reactions on ^{92}Mo, ^{94}Mo, and ^{95}Mo leading to the production of ^{91m}Nb to TALYS calculations (see Fig. 1 for description).

IV. CONCLUSION

Production cross sections for 33 proton-induced reactions resulting in the formation of radioactive technetium,

niobium, and molybdenum were measured in the proton energy range of 8–19 MeV. Nine of the cross sections measured in this work, ^{92}Mo$(p, n)^{92}$Tc, ^{92}Mo$(p, g)^{93m}$Tc, ^{92}Mo$(p, g)^{93g}$Tc, ^{97}Mo$(p, n)^{97m}$Tc, ^{98}Mo$(p, 2n)^{97m}$Tc, ^{92}Mo$(p, pn)^{91(m+g)}$Mo, ^{94}Mo$(p, pn)^{93m}$Mo, ^{92}Mo$(p, 2p)^{91}$Nb, ^{94}Mo$(p, \alpha)^{91m}$Nb, represent the first detailed investigation in this energy region. In all cases, the present measurements were compared to the available literature as well as the results from the statistical model code TALYS-1.8.

Comparison between the experimental data and the predictions of TALYS for the various (p, xn) reactions typically shows fair agreement both in shape and absolute value. Some discrepancy appears in the predictions for isomer-ground state pairs (e.g., ^{94}Tc). TALYS tends to have more variance in shape and amplitude for reactions with charged particles in the exit channel, occasionally dramatically over- or underestimating the experimental cross section [^{94}Mo$(p, pn)^{93m}$Mo, and ^{100}Mo$(p, pn)^{99}$Mo respectively].

One notable exception to the generally favorable results of TALYS is the well studied ^{100}Mo$(p, 2n)^{99m}$Tc. In this case TALYS significantly underproduces ^{99m}Tc above 11 MeV. The measured ^{99m}Tc cross section from this work confirms the divergence seen between literature and statistical model codes, and in particular supports the recent measurements of Červenák and Lebeda [32] suggesting that the measurements of Gagnon *et al.* [11] and others may overestimate the production of this important medical radioisotope.

The results from this work are meaningful for the feasibility of cyclotron ^{99m}Tc production. Along with providing an updated estimate of the amplitude of the main cross section forming ^{99m}Tc, the individual cross sections leading to other technetium isotopes can be used to directly calculate increased dose associated with a certain target irradiation. Cross sections which vary from statistical model calculated values (e.g., ^{97m}Tc) represent reactions where the potential impact on patient health may be underestimated. Additionally, the production cross sections for molybdenum and niobium from this study can be used to estimate the potential for target recycling postirradiation.

ACKNOWLEDGMENTS

This work was supported by NSF under Grants No. PHY-1713857 (Nuclear Science Laboratory) and No. PHY-1614442, and by the NRC under Grant No. NRC-HQ-12-G-38-0073. This work was also supported in part by the University of Notre Dame Center for Research Computing (CRC).

[1] Nuclear Energy Agency Technical Report No. NEA/SEN/HLGMR(2018)3, OECD, Paris, 2018 (unpublished).
[2] H. Bonet, B. David, and B. Ponsard, Technical Report, 2005 (unpublished).
[3] W. C. Eckelman, JACC: Cardiovascular Imaging **2**, 364 (2009).
[4] International Atomic Energy Agency, *Production Technologies for Molybdenum-99 and Technetium-99m*, IAEA-TECDOC-1065 (IAEA, Vienna, 1999).
[5] M. R. A. Pillai, A. Dash, and F. F. R. Knapp, J. Nucl. Med. **54**, 313 (2013).
[6] R. Van Noorden, Nature (London) **504**, 202 (2013).
[7] A. Lokhov, Nuclear Energy Agency Technical Report, 2010 (unpublished).
[8] M. C. Lagunas-Solar, P. M. Kiefer, O. F. Carvacho, C. A. Lagunas, and Y. P. Cha, Int. J. Radiat. Appl. Instrum. Part A **42**, 643 (1991).
[9] B. Scholten, R. M. Lambrecht, M. Cogneau, H. V. Ruiz, and S. M. Qaim, Appl. Radiat. Isot. **51**, 69 (1999).
[10] B. Guérin, S. Tremblay, S. Rodrigue, J. A. Rousseau, V. Dumulon-Perreault, R. Lecomte, J. E. van Lier, A. Zyuzin, and E. J. van Lier, J. Nucl. Med. **51**, 13N (2010).
[11] K. Gagnon, F. Bénard, M. Kovacs, T. J. Ruth, P. Schaffer, J. S. Wilson, and S. A. McQuarrie, Nucl. Med. Biol. **38**, 907 (2011).
[12] S. M. Qaim, S. Sudár, B. Scholten, A. J. Koning, and H. H. Coenen, Appl. Radiat. Isot. **85**, 101 (2014).
[13] International Atomic Energy Agency, IAEA Radioisotopes and Radiopharmaceuticals Report No. 2, IAEA, Vienna, 2017 (unpublished).
[14] S. V. Selivanova, E. Lavallee, H. Senta, L. Caouette, J. A. Sader, E. J. van Lier, A. Zyuzin, J. E. van Lier, B. Guerin, E. Turcotte, and R. Lecomte, J. Nucl. Med. **56**, 1600 (2015).
[15] N. M. Uzunov, L. Melendez-Alafort, M. Bello, G. Cicoria, F. Zagni, L. De Nardo, A. Selva, L. Mou, C. Rossi-Alvarez, G. Pupillo, G. Di Domenico, L. Uccelli, A. Boschi, F. Groppi, A. Salvini, A. Taibi, A. Duatti, P. Martini, M. Pasquali, M. Loriggiola *et al.*, Phys. Med. Biol. **63**, 185021 (2018).
[16] O. Lebeda, E. J. van Lier, J. Štursa, J. Ráliš, and A. Zyuzin, Nucl. Med. Biol. **39**, 1286 (2012).
[17] J. Esposito, G. Vecchi, G. Pupillo, A. Taibi, L. Uccelli, A. Boschi, and M. Gambaccini, Sci. Technol. Nucl. Install. **2013**, 972381 (2013).
[18] X. Hou, J. Tanguay, K. Buckley, P. Schaffer, F. Bénard, T. J. Ruth, and A. Celler, Phys. Med. Biol. **61**, 542 (2016).
[19] M. Beard, E. Uberseder, R. Crowter, and M. Wiescher, Phys. Rev. C **90**, 034619 (2014).
[20] T. Rauscher, R. D. Hoffman, S. E. Woosley, and F.-K. Thielemann, in *Capture Gamma-Ray Spectroscopy and Related Topics: 10th International Symposium*, edited by S. Wender and S. Kelley, AIP Conf. Proc. No. 529 (AIP, Melville, NY, 2000), pp. 331–338.
[21] J. Pereira and F. Montes, Phys. Rev. C **93**, 034611 (2016).
[22] M. E. Wieser and J. R. D. Laeter, Phys. Rev. C **75**, 055802 (2007).
[23] J. F. Ziegler, M. Ziegler, and J. Biersack, Nucl. Instrum. Methods Phys. Res. B **268**, 1818 (2010).
[24] F. Tárkányi, F. Ditrói, A. Hermanne, S. Takács, and A. V. Ignatyuk, Nucl. Instrum. Methods Phys. Res. B **280**, 45 (2012).
[25] S. Agostinelli, J. Allison, K. Amako, J. Apostolakis, H. Araujo, P. Arce, M. Asai, D. Axen, S. Banerjee, G. Barrand, F. Behner, L. Bellagamba, J. Boudreau, L. Broglia, A. Brunengo, H. Burkhardt, S. Chauvie, J. Chuma, R. Chytracek, G. Cooperman *et al.*, Nucl. Instrum. Methods Phys. Res. A **506**, 250 (2003).

[26] G. Gilmore, *Practical Gamma-Ray Spectrometry*, 2nd ed. (Wiley, West Sussex, England, 2008).
[27] R. S. Tilbury, *Activation Analysis with Charged Particles* (National Academy of Sciences, Tuxedo, NY, 1988).
[28] National Nuclear Data Center, Nuclear structure and decay Data (NuDat 2.7), Brookhaven National Laboratory, http://www.nndc.bnl.gov/nudat2/.
[29] S. Manenti, U. Holzwarth, M. Loriggiola, L. Gini, J. Esposito, F. Groppi, and F. Simonelli, Appl. Radiat. Isot. **94**, 344 (2014).
[30] M.-M. Bé, V. Chisté, C. Dulieu, E. Browne, V. Chechev, N. Kuzmenco, R. Helmer, A. Nichols, E. Schönfeld, and R. Dersch, *Table of Radionuclides*, Monographie BIPM-5 (Vol. 1-A= 1 to 150) (Bureau International des Poids et Mesures, Sèvres, France, 2004), https://www.bipm.org/utils/common/pdf/monographieRI/Monographie_BIPM-5_Tables_Vol1.pdf.
[31] D. Yuan and W. Kernan, J. Appl. Phys. **101**, 094907 (2007).
[32] J. Červenák and O. Lebeda, Nucl. Instrum. Methods Phys. Res. B **380**, 32 (2016).
[33] O. Lebeda and M. Pruszyński, Appl. Radiat. Isot. **68**, 2355 (2010).
[34] S. Takács, A. Hermanne, F. Ditrói, F. Tárkányi, and M. Aikawa, Nucl. Instrum. Methods Phys. Res. B **347**, 26 (2015).
[35] L. Wolfenstein, Phys. Rev. **82**, 690 (1951).
[36] W. Hauser and H. Feshbach, Phys. Rev. **87**, 366 (1952).
[37] M. Herman, R. Capote, B. Carlson, P. Obložinský, M. Sin, A. Trkov, H. Wienke, and V. Zerkin, Nucl. Data Sheets **108**, 2655 (2007).
[38] A. J. Koning, S. Hilaire, and M. C. Duijvestijn, in *ND2007* (EDP Sciences, Nice, France, 2007).
[39] A. Koning, S. Hilaire, and S. Goriely, "TALYS-1.8 A nuclear reaction program: User Manual", 2015.
[40] A. Celler, X. Hou, F. Bénard, and T. Ruth, Phys. Med. Biol. **56**, 5469 (2011).
[41] See Supplemental Material at http://link.aps.org/supplemental/10.1103/PhysRevC.100.034614 for a complete set of figures for all of the measured cross sections in this work as well as an example of a TALYS input file. The Supplemental Material contains Refs. [55–59].
[42] S. Takács, F. Tárkányi, M. Sonck, and A. Hermanne, Nucl. Instrum. Methods Phys. Res. B **198**, 183 (2002).
[43] J. Tanguay, X. Hou, P. Esquinas, M. Vuckovic, K. Buckley, P. Schaffer, F. Bénard, T. J. Ruth, and A. Celler, Phys. Med. Biol. **60**, 8229 (2015).
[44] A. A. Alharbi, A. Azzam, A. Banu, A. Spiridon, B. Roeder, E. Simmons, L. Trache, M. McCleskey, R. E. Tribble, and V. Z. Goldberg, *Medical Radioisotopes Production: A Comprehensive Cross-Section Study for the Production of Mo and Tc Radioisotopes via Proton Induced Nuclear Reactions on natMo* (IntechOpen, Rijeka, 2011).
[45] M. B. Challan, M. N. H. Comsan, and M. A. Abou-Zeid, J. Nucl. Radiat. Phys **2**, 1 (2007).
[46] M. U. Khandaker, M. S. Uddin, K. S. Kim, Y. S. Lee, and G. N. Kim, Nucl. Instrum. Methods Phys Res B **262**, 171 (2007).
[47] M. U. Khandaker, A. Meaze, K. Kim, D. Son, G. Kim, and Y. S. Lee, J. Korean Phys. Soc. **48**, 821 (2006).
[48] M. Lagunas-Solar, Technical Report No. IAEA-TECDOC-1065, International Atomic Energy Agency, Vienna, 87-112, 1999 (unpublished).
[49] V. N. Levkovskij, *Middle Mass Nuclides (A= 40–100) Activation Cross-sections by Medium Energy (E= 10–50 MeV) Protons and Alpha Particles (Experiment and Systematics)* (Inter-vesi, Moscow, 1991).
[50] S. Takács, Z. Szűcs, F. Tárkányi, A. Hermanne, and M. Sonck, J. Radiol. Nucl. Chem. **257**, 195 (2003).
[51] P. Chodash, C. T. Angell, J. Benitez, E. B. Norman, M. Pedretti, H. Shugart, E. Swanberg, and R. Yee, Appl. Radiat. Isot. **69**, 1447 (2011).
[52] W. Zhao, W. Yu, X. Han, and H. Lu, Communication of nuclear data progress (CN9901266) **19**, 17 (1998).
[53] S. Takács, F. Ditrói, M. Aikawa, H. Haba, and N. Otuka, Nucl. Instrum. Methods Phys. Res. B **375**, 60 (2016).
[54] K. Gagnon, J. S. Wilson, C. M. B. Holt, D. N. Abrams, A. J. B. McEwan, D. Mitlin, and S. A. McQuarrie, Appl. Radiat. Isot. **70**, 1685 (2012).
[55] P. J. Daly, B. M. Seppelt, and P. F. D. Shaw, Nucl. Phys. A **119**, 673 (1968).
[56] M. Izumo, H. Matsuoka, T. Sorita, Y. Nagame, T. Sekine, K. Hata, and S. Baba, Int. J. Radiat. Appl. Instrum. Part A **42**, 297 (1991).
[57] E. Skakun, V. Batij, Y. Rakivnenko, and O. Rastrepin, Sov. J. Nucl. Phys. **46**, 17 (1987).
[58] F. Rösch and S. M. Qaim, Radiochimica Acta **62**, 115 (1993).
[59] K. Gagnon, J. S. Wilson, and S. A. McQuarrie, Nucl. Med. Biol. **39**, 923 (2012).